Journal of Thermal Analysis and Calorimetry (2025) 150:16123–16138
https://doi.org/10.1007/s10973-025-14670-2

Boundary layer flow and heat transfer of penta-hybrid nanofluid over a permeable slip stretching/shrinking sheet: numerical analysis with logic mining via S2SATRA

Nur Syahirah Wahid[1] · Nurul Atiqah Romli[2] · Nur Ezlin Zamri[1] · Shahirah Abu Bakar[3] · Nor Ain Azeany Mohd Nasir[4,5] · Siti Zulaikha Mohd Jamaludin[2] · Mohd Shareduwan Mohd Kasihmuddin[2] · Mohd. Asyraf Mansor[6] · Norihan Md Arifin[1,4] · Ioan Pop[7,8]

Received: 25 December 2024 / Accepted: 6 August 2025 / Published online: 6 September 2025

Abstract

This study investigates the boundary layer flow of penta-hybrid nanofluid with suction and velocity slip over a stretching/shrinking sheet. The exploration of penta-hybrid nanofluid, which consist of five different nanoparticles, is motivated by the synergistic effects that enhance heat transfer performance. A mathematical model is formulated in the form of partial differential equations based on the fluid flow configuration, which are then reduced to ordinary differential equations and solved numerically using the finite difference scheme in MATLAB. Dual solutions are obtained, and the impacts of various parameters are analyzed. This study demonstrates that penta-hybrid nanofluid with a high concentration of titanium dioxide significantly enhances the heat transfer rate compared to those with lower concentrations, particularly when operating under conditions of lower suction and velocity slip at the boundary, with the sheet in a stretching condition. Additionally, the increase in suction and velocity slip allows the sheet to shrink more extensively, which helps delay boundary layer separation and prevents the turbulent flow. Furthermore, Supervised 2 Satisfiability Reverse Analysis (S2SATRA) is employed to understand parameter interactions and optimize heat transfer performance. The analysis identifies the best-induced logic for accurately predicting the heat transfer rate, which is expressed as: $\mathrm{Re}_x^{-1/2}\mathrm{Nu}_x = (\lambda \vee \phi_5) \wedge (\phi_2 \vee \phi_1) \wedge (\phi_3 \vee \neg\phi_4)$ and $\mathrm{Re}_x^{-1/2}\mathrm{Nu}_x = (S \vee \phi_4) \wedge (\lambda \vee \neg\phi_3) \wedge (A \vee \phi_5)$.

Keywords Boundary layer · Penta-hybrid nanofluid · Stretching/shrinking · Velocity slip · S2SATRA

List of symbols

a	Positive constant
A	Velocity slip parameter
A_1	Velocity slip factor
C_f	Skin friction coefficient
k_{phnf}	Thermal conductivity of the penta-hybrid nanofluid
ϕ_i	Nanoparticle volume fractions
Pr	Prandtl number
λ	Stretching/shrinking parameter
μ_{phnf}	Dynamic viscosity of the penta-hybrid nanofluid
Nu_x	Local Nusselt number
ρ_{phnf}	Density of the penta-hybrid nanofluid

✉ Nur Syahirah Wahid
syahirahwahid@upm.edu.my

1 Department of Mathematics and Statistics, Faculty of Science, Universiti Putra Malaysia, 43400 UPM Serdang, Selangor, Malaysia

2 School of Mathematical Sciences, Universiti Sains Malaysia, 11800 USM Penang, Malaysia

3 Takasago Thermal/Environmental Systems Laboratory, Malaysia–Japan International Institute of Technology, Universiti Teknologi Malaysia, 54100 Kuala Lumpur, Malaysia

4 Institute for Mathematical Research, Universiti Putra Malaysia, 43400 UPM Serdang, Selangor, Malaysia

5 Department of Mathematics, Centre for Defence Foundation Studies, Universiti Pertahanan Nasional Malaysia, Kem Sungai Besi, 57000 Kuala Lumpur, Malaysia

6 School of Distance Education, Universiti Sains Malaysia, 11800 USM Penang, Malaysia

7 Department of Mathematics, Babeş-Bolyai University, R-400084 Cluj-Napoca, Romania

8 Academy of Romanian Scientists, 3 Ilfov Street, 050044 Bucharest, Romania

$(\rho C_p)_{phnf}$	Heat capacity of the penta-hybrid nanofluid
Re_x	Local Reynolds number
S	Suction
T_∞	Far-field temperature
T_w	Surface temperature
T	Temperature
u, v	Velocity components
u_w	Velocity of the sheet
v_w	Wall mass transfer velocity
x, y	Cartesian coordinates

Introduction

Nanotechnology has revolutionized various fields in manipulating matter at the nanoscale, including fluid mechanics and heat transfer. The assortment of nanoparticles in base fluids has led to the development of nanofluid, which exhibit significantly enhanced thermophysical properties compared to conventional fluids. These enhanced properties, such as increased thermal conductivity and convective heat transfer coefficient, make nanofluid promising candidates for numerous applications, including heat exchangers [1], solar energy systems [2], and electronics cooling [3]. While nanofluid have shown remarkable potential, recent research has explored the possibility of further improving their performance by incorporating multiple types of nanoparticles into a single base fluid. This approach, known as hybrid nanofluid technology, has yielded even more substantial enhancements in thermophysical properties. The enhancement in hybrid nanofluid has been explored by Khan et al. [4], Mishra et al. [5], Sarkar et al. [6], and Khalili Najafabadi et al. [7], to name a few. Based on their findings, combining different nanoparticles can result in synergistic effects, leading to enhanced heat transfer capabilities surpassing individual nanofluid. Building upon the success of hybrid nanofluid, researchers have ventured into multi-component nanofluid, also known as penta-hybrid nanofluid. These fluids contain five distinct types of nanoparticles suspended in a base fluid. The introduction of additional nanoparticle components offers the potential for further tailoring the thermophysical properties of the fluid, enabling it to meet specific engineering requirements. The study of penta-hybrid nanofluid flow and heat transfer is a relatively new and emerging area of research. Gomathi and Poulomi [8] have recently investigated the penta-hybrid nanofluid flow and heat transfer with the Casson–Williamson model. They consider silver, gold, titanium dioxide, magnesium oxide, and copper as penta-nanoparticles dissolved in ethyl glycol as a base fluid. They reported that the penta-hybrid nanofluid enhanced by more than 60% while minimizing the energy loss to more than 200%. With these findings, exploring penta-hybrid nanofluid flow and heat transfer is wise. By investigating the factors that influence heat transfer enhancement, such as nanoparticle concentration, size distribution, and fluid properties, researchers can develop guidelines for designing and utilizing penta-hybrid nanofluid in various applications.

The suction effect on the surface, which is a surface that draws fluid away from the flow boundary, can be a powerful tool for controlling the flow and heat transfer characteristics. The suction effect can be applied to the surface to reduce the boundary layer thickness, which in turn enhances the heat transfer. This occurrence is due to the fact that a thinner boundary layer promotes heat transfer and reduces drag. For specific problems, suction can help prevent boundary layer separation, which occurs when the fluid flow reverses direction near the surface. Separation can lead to a significant reduction in heat transfer and an increase in drag. Several researchers with various problems have included suction effects, such as Alharbi [9], Paul et al. [10], Samat et al. [11], and Jaafar et al. [12]. From their findings, by removing the low-energy fluid near the surface, suction can promote the movement of higher-energy fluid toward the surface, leading to increased convective heat transfer. The combination of reduced boundary layer thickness and enhanced convective heat transfer can improve a system's overall thermal performance. Wahid et al. [13] show evidence of this claim that incrementing the suction by 4% will increase the delay of boundary layer separation by 9%. It is vital to delay the separation and help stabilize the flow to halt the turbulence, which can be beneficial in specific applications where stable flow is required. Suction also can be used to modify the velocity profile of the fluid flow. By controlling the suction rate, achieving desired flow characteristics, such as uniform velocity profiles or specific flow patterns, is possible. Hammoodi et al. [14] have drawn attention to this statement, where the suction reduced the velocity field and the fluid diffusion in their research. However, Sarma and Paul [15] reveal that the suction rate leads to higher flow resistance due to fluid removal near the surface, while the stretching parameter has the opposite effect, reducing flow resistance. These factors positively influence heat and mass transfer rates at higher values, indicating that enhanced convective transport is more pronounced with increased suction and stretching.

Interfacial phenomena, such as slip velocity, often influence the flow behavior of nanofluid. Traditional slip models assume a linear relationship between the slip velocity and the shear stress at the fluid–solid interface. While this approach has been widely used, it may not accurately capture the complex interactions between the nanoparticles and the fluid in specific scenarios. On the other hand, first-order slip models consider a more general relationship between slip velocity and shear stress, incorporating first-order terms that can account for nonlinear effects. A number of studies, including Badiger et al. [16], Memon et al. [17], Fatima et al. [18] and Jamrus et al. [19], have investigated the impact of first-order slip on different fluid flow problems. By considering first-order terms in the slip velocity expression, first-order models can provide more accurate predictions of fluid velocity, temperature distribution, and heat transfer rates. The effect of first-order slip is essential for designing and optimizing heat transfer systems. The effect of first-order slip when the surface is shrunk is worth investigating. The investigation was carried out by Hashim et al. [20], who reported that the velocity slip parameter at the interface exhibited a sharp increase, leading to a controlled upward or forward motion. This outcome corresponded to a negative lambda value, indicating a shrinking surface area in the system. Mahmood et al. [21] mentioned in their findings that the mixed convection parameter enhances the friction coefficient on the stretched vertical surface. However, its effect is counteracted by the presence of magnetic, mass suction, and velocity slip parameters. Another investigation has been done by Panda et al. [22], which indicates that first-order slip creates a discrepancy between the surface velocity and the fluid velocity, with increasing slip leading to a gradual increase in the velocity profile regardless of suction or injection variations. Recently, Usafzai et al. [23] also considered velocity slip in their model of ternary hybrid nanofluid and obtained multiple exact solutions.

The study of fluid flow and heat transfer over a shrinking sheet has gained substantial attention in recent years due to its diverse applications in various engineering and industrial processes. As the name implies, a shrinking sheet is a surface that contracts with time. This phenomenon is observed in several real-world scenarios, such as polymer processing, metallurgy, and manufacturing of continuous sheets. Mahabaleshwar et al. [24], Mahros and Aly [25], Roy et al. [26], and Kaswan et al. [27] are among many researchers who have been exploring the research on shrinking sheets on fluid flow and heat transfer. The impact of a shrinking sheet on fluid flow and heat transfer is multifaceted. The contraction of the surface induces a boundary layer flow near the sheet, which can significantly alter the velocity and temperature profiles of the fluid. This interaction can lead to exciting and complex flow phenomena, including boundary layer separation, recirculation zones, and heat transfer enhancement. When Rafique et al. [28] solved their problem, they found that local skin friction increases when there is more unsteadiness, nanoparticle volume fraction, magnetic field, porous medium, and strain rate ratio on the shrinking surface. Alkasasbeh and Mohamed [29] found that a higher magnetic parameter in the SWCNT + MCWNT hybrid nanofluid will make the skin friction increase by 72.2% compared to SWCNT nanofluid on the surface that is getting smaller. Jain et al. [30] also reported that shrinking parameters will affect the velocity profile's amplification.

Therefore, as reviewed in the literature, the investigation of boundary layer flow in nanofluid has evolved from single-phase nanofluid to hybrid nanofluid, and now to penta-hybrid nanofluid, which consists of five different nanoparticles. This hybridization is primarily driven by the synergistic effects that improve heat transfer performance when nanoparticles are combined. Additionally, the literature highlights that incorporating parameters such as suction and velocity slip can effectively control the system, particularly under the conditions of stretching and shrinking sheets, which are commonly encountered in various engineering applications. Given this, it is essential to first model and numerically simulate these conditions before they can be applied in real-world scenarios. This study, therefore, aims to formulate a mathematical model for the boundary layer flow of penta-hybrid nanofluid with suction and velocity slip over a stretching/shrinking sheet and simulates the solutions. This study provides dual solutions and offers insights into regulating the velocity, temperature, skin friction, heat transfer rate, and boundary layer separation of penta-hybrid nanofluid. The numerical results are further analyzed using S2SATRA to explore the interactions between the parameters specifically on the optimization of the heat transfer rate, as a guide on proper adjustment of the control parameters.

Mathematical formulation

We consider the two-dimensional steady boundary layer flow of an incompressible penta-hybrid nanofluid along a permeable stretching/shrinking sheet, as it is shown in Fig. 1, where the Cartesian coordinates (x, y) are measured along the surface of the sheet and normal to it, respectively. The wall mass transfer velocity is denoted by $v_{\mathrm{w}} = -\sqrt{a\nu_{\mathrm{f}}}S$ with positive values of S indicating suction effect while the velocity of the stretching/shrinking sheet is $u_{\mathrm{w}}(x) = ax$, where a is constant. The velocity slip factor is denoted by A_1, the temperature of the far field and at the surface is denoted as T_∞ and y T_{w}, respectively.

Given these assumptions, the governing models consisting of continuity, momentum, and energy equations are formulated as follows (see Devi and Devi [31]; Waini et al. [32]; Wahid et al. [33]):

$$\frac{\partial u}{\partial x} + \frac{\partial v}{\partial y} = 0, \tag{1}$$

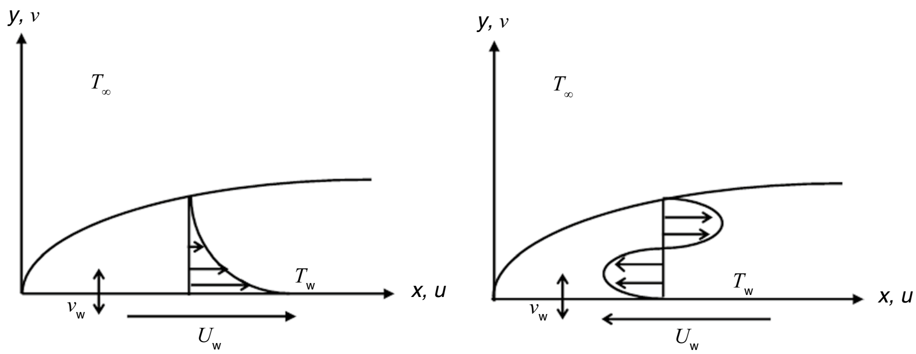

Fig. 1 Flow model over stretching (left) and shrinking (right) sheet

Table 1 The model of thermophysical properties [8, 34, 35]

Properties	Model
Dynamic viscosity	$\mu_{\text{phnf}} = \frac{\mu_{\text{f}}}{(1-\phi_1)^{2.5}(1-\phi_2)^{2.5}(1-\phi_3)^{2.5}(1-\phi_4)^{2.5}(1-\phi_5)^{2.5}}$
Density	$\rho_{\text{phnf}} = (1-\phi_5)\left((1-\phi_4)\left((1-\phi_3)\left((1-\phi_2)\left((1-\phi_1)\rho_{\text{f}} + \phi_1\rho_1\right) + \phi_2\rho_2\right) + \phi_3\rho_3\right) + \phi_4\rho_4\right) + \phi_5\rho_5$
Heat capacitance	$(\rho C_{\text{p}})_{\text{phnf}} = (1-\phi_5)\left((1-\phi_4)\left((1-\phi_3)\left((1-\phi_2)\left((1-\phi_1)(\rho C_{\text{p}})_{\text{f}} + \phi_1(\rho C_{\text{p}})_1\right) + \phi_2(\rho C_{\text{p}})_2\right) + \phi_3(\rho C_{\text{p}})_3\right) + \phi_4(\rho C_{\text{p}})_4\right) + \phi_5(\rho C_{\text{p}})_5$
Thermal conductivity	$k_{\text{phnf}} = \frac{k_5 + 2k_{\text{tehnf}} - 2\phi_5(k_{\text{tehnf}} - k_5)}{k_5 + 2k_{\text{tehnf}} + \phi_5(k_{\text{tehnf}} - k_5)} \times k_{\text{tehnf}}$
	Where
	$k_{\text{tehnf}} = \frac{k_4 + 2k_{\text{thnf}} - 2\phi_4(k_{\text{thnf}} - k_4)}{k_4 + 2k_{\text{thnf}} + \phi_4(k_{\text{thnf}} - k_4)} \times k_{\text{thnf}}$
	$k_{\text{thnf}} = \frac{k_3 + 2k_{\text{hnf}} - 2\phi_3(k_{\text{hnf}} - k_3)}{k_3 + 2k_{\text{hnf}} + \phi_3(k_{\text{hnf}} - k_3)} \times k_{\text{hnf}}$
	$k_{\text{hnf}} = \frac{k_2 + 2k_{\text{nf}} - 2\phi_2(k_{\text{nf}} - k_2)}{k_2 + 2k_{\text{nf}} + \phi_2(k_{\text{nf}} - k_2)} \times k_{\text{nf}}$
	$k_{\text{nf}} = \frac{k_1 + 2k_{\text{f}} - 2\phi_1(k_{\text{f}} - k_1)}{k_1 + 2k_{\text{f}} + \phi_1(k_{\text{f}} - k_1)} \times k_{\text{f}}$

Table 2 Value of thermophysical properties (Gomathi and Poulomi [8])

Properties	H_2O	Ag	Au	MgO	Cu	TiO_2
$\rho/\text{kg m}^{-3}$	997.1	10,500	19,320	3580	8933	4250
$C_{\text{p}}/\text{J kg}^{-1}\text{K}^{-1}$	4179	235	129	960	385	686.2
$k/\text{W m}^{-1}K^{-1}$	0.613	429	314	48.4	400	8.9538
Pr	6.2	NA	NA	NA	NA	NA

$$u\frac{\partial u}{\partial x} + v\frac{\partial u}{\partial y} = \frac{\mu_{\text{phnf}}}{\rho_{\text{phnf}}}\frac{\partial^2 u}{\partial y^2}, \tag{2}$$

$$u\frac{\partial T}{\partial x} + v\frac{\partial T}{\partial y} = \frac{k_{\text{phnf}}}{(\rho C_{\text{p}})_{\text{phnf}}}\frac{\partial^2 T}{\partial y^2}, \tag{3}$$

$$u = U_w(x) = \lambda u_w(x) + A_1 \frac{\partial u}{\partial y}, v = v_w \text{ at } y = 0, u \to 0 \text{ as } y \to \infty$$
$$T = T_w \text{ at } y = 0, T \to T_\infty \text{ as } y \to \infty, \tag{4}$$

where (u, v) are the velocity components along (x, y)—axes, and T is the temperature of the penta-hybrid nanofluid. It should be noted here that μ_{phnf} is the dynamic viscosity, ρ_{phnf} is the density, k_{phnf} is the thermal conductivity, and $(\rho C_p)_{phnf}$ is the heat capacity of the penta-hybrid nanofluid which the formulations are provided in Table 1. Additionally, Eq. (4) represents the condition at the boundary that has a permeable surface, allowing fluid suction or injection along the y-axis (normal to the sheet). Meanwhile, the boundary is also shrinking or stretching along the x-axis, where velocity slip condition is also applied.

Here, ϕ_i, $(i = 1, 2, 3, 4, 5)$ are the nanoparticle volume fractions such that the subscripts of 1, 2, 3, 4, and 5 refer to silver, gold, magnesium oxide, copper and titanium dioxide nanoparticles, respectively. The subscript of *phnf*, *tehnf*, *thnf*, *hnf*, *nf*, and *f* refer to the penta-hybrid nanofluid, tetra-hybrid nanofluid, tri-hybrid nanofluid, di-hybrid nanofluid, mono-nanofluid, and base fluid, respectively. The physical properties of the base fluid are tabulated in Table 2. The hybridization of these Ag, Au, MgO, Cu, and TiO_2 nanoparticles are preferred due to their synergistic effects, where each nanoparticle contributes uniquely to enhance the thermal and physical properties of the penta-hybrid nanofluid. For example, metals like Cu, Ag, and Au offer excellent thermal conductivity, while metal oxides like TiO_2 and MgO provide stability and cost-effectiveness. The combination helps improve overall heat transfer performance. Additionally, these types of nanoparticles have already been used in the literature, which proves their significant.

To reduce the complexity of the model, the similarity variables are introduced, such that [32, 36]:

$$u = axf'(\eta),\ v = -\sqrt{a\nu_f}f(\eta),\ T = \theta(\eta)(T_w - T_\infty) + T_\infty,\ \eta = y\sqrt{\frac{a}{\nu_f}}. \tag{5}$$

By applying the similarity variables from Eq. (5) to Eqs. (2)–(4), the model reduces to the following boundary value problems in the form of ODEs, such that:

$$\left(\frac{\mu_{phnf}/\mu_f}{\rho_{phnf}/\rho_f}\right)f''' - f'^2 + ff'' = 0, \tag{6}$$

$$\frac{1}{\Pr}\left(\frac{k_{phnf}/k_f}{(\rho C_p)_{phnf}/(\rho C_p)_f}\right)\theta'' + f\theta' = 0, \tag{7}$$

$$f(0) = S, f'(0) = \lambda + Af''(0), f'(\infty) \to 0$$
$$\theta(0) = 1, \theta(\infty) \to 0, \tag{8}$$

where Pr is the Prandtl number, $S > 0$ is the suction parameter, A is the first-order velocity slip parameter, and λ is the stretching/shrinking parameter, with $\lambda > 0$ for stretching, $\lambda < 0$ for shrinking and $\lambda = 0$ for static sheet. These parameters can be defined as:

$$\Pr = \frac{(\mu C_p)_f}{k_f},\ A = A_1\sqrt{\frac{a}{\nu_f}}. \tag{9}$$

The model generates numerical solutions in the form of physical quantities, specifically the skin friction coefficient C_f and the local Nusselt number Nu_x, defined as follows:

$$C_f = \frac{\mu_{phnf}}{\rho_f u_w^2(x)}\left(\frac{\partial u}{\partial y}\right)_{y=0}, Nu_x = \frac{xk_{phnf}}{k_f(T_w - T_\infty)}\left(-\frac{\partial T}{\partial y}\right)_{y=0}, \tag{10}$$

Using Eq. (5), Eq. (10) transforms to:

$$Re_x^{1/2}C_f = \frac{\mu_{phnf}}{\mu_f}f''(0), Re_x^{-1/2}Nu_x = -\frac{k_{phnf}}{k_f}\theta'(0), \tag{11}$$

where $Re_x = u_w x/\nu_f$ is the local Reynolds number.

Table 3 Comparison value of solutions when $\lambda = 1$, $\phi_1 = 0.1$, $\phi_3 = \phi_4 = \phi_5 = S = A = 0$, $\Pr = 6.135$, $\rho_f = 997$, $(C_p)_f = 4180$, $k_f = 0.6071$

ϕ_2	$Re_x^{1/2}C_f$		$Re_x^{-1/2}Nu_x$	
	Present	Waini et al. [32]	Present	Waini et al. [32]
0.005	− 1.327097964	− 1.327098	1.961773022	1.961769
0.02	− 1.409490197	1.409490	1.989307591	1.989304
0.04	− 1.520721213	− 1.520721	2.026446497	2.026442
0.06	− 1.634118688	− 1.634119	2.064150414	2.064146
0.1	− 1.869763894	− 1.869764	2.141648481	2.141644

Table 4 Values of $\mathrm{Re}_x^{1/2}C_f$ and $\mathrm{Re}_x^{-1/2}\mathrm{Nu}_x$ when $\lambda = 1$ and $\phi_1 = \phi_2 = \phi_3 = \phi_4 = 0.005$

S	A	ϕ_5	$\mathrm{Re}_x^{1/2}C_f$		$\mathrm{Re}_x^{-1/2}\mathrm{Nu}_x$	
			1st	2nd	1st	2nd
0.3	1	0.005	− 0.518861147	− 0.528879796	2.669383216	2.649593836
0.4	1	0.005	− 0.535128429	− 0.548380027	3.169838988	3.146330050
0.5	1	0.005	− 0.551449054	− 0.568741158	3.690552187	3.662942387
0.5	2	0.005	− 0.350791951	− 0.360922151	3.541789287	3.509220149
0.5	3	0.005	− 0.259277251	− 0.266531907	3.459510570	3.423725234
0.5	3	0.010	− 0.262565987	− 0.269912828	3.458070227	3.421868102
0.5	3	0.015	− 0.265903738	− 0.273343530	3.456674425	3.420057496
0.5	1	0.005	− 0.551449054	− 0.568741158	3.690552187	3.662942387
0.5	1	0.010	− 0.558447755	− 0.575959612	3.690675375	3.662730439
0.5	1	0.015	− 0.565536124	− 0.583269483	3.690846894	3.662568053

Results and discussion

The fluid flow problem in this study was initially modeled using PDEs, which were subsequently transformed into ODEs. These ODEs were solved using MATLAB's bvp4c solver, which employs a finite difference scheme based on the Lobatto IIIa formula. The solver was configured with zero relative tolerance, and the maximum boundary layer thickness was set to $\eta_\infty = 25$. The boundary layer thickness was set to 25 to ensure the boundary conditions at infinity are properly fulfilled. This value is not typical, as it depends on the model and the ability to generate accurate numerical solutions. A smaller value would prevent the solution from fully satisfying the far-field conditions. Two distinct initial guesses were employed to obtain two non-unique solutions. The ODEs were reduced to first-order equations using specific assumptions to align with the solver requirements in MATLAB, such that:

$$f = y(1), f' = y(2), f'' = y(3), \theta = y(4), \theta' = y(5). \tag{12}$$

Hence, Eqs. (6)–(8) become:

$$f''' = \left(\frac{\rho_{\mathrm{phnf}}/\rho_f}{\mu_{\mathrm{phnf}}/\mu_f}\right)(y(2)y(2) - y(1)y(3)), \tag{13}$$

$$\theta'' = \frac{1}{\frac{1}{\mathrm{Pr}}\left(\frac{k_{\mathrm{phnf}}/k_f}{(\rho C_p)_{\mathrm{phnf}}/(\rho C_p)_f}\right)}(-y(1)y(5)), \tag{14}$$

$$\begin{aligned} &ya(1) - S,\ ya(2) - \lambda - Aya(3),\ yb(2), \\ &ya(4) - 1,\ yb(4), \end{aligned} \tag{15}$$

where ya and yb refer to the boundary conditions as when $\eta = 0$ and $\eta \to \infty$, respectively.

Before generating solutions to analyze the impact of parameters on the fluid flow system, it is crucial to validate the model by comparing the present results with existing, comparable results. This step ensures that the model is both correctly implemented in the solver and accurately solved. The comparison of results between the present model and the existing model is presented in Table 3. The results show good agreement, providing confidence to proceed to the next step, that is generating solutions for the current problem model.

The solution to the current problem is presented in terms of velocity (measured by $f'(\eta)$), temperature (measured by $\theta(\eta)$), skin friction (measured using $\mathrm{Re}_x^{1/2}C_f$), and heat transfer rate (measured using $\mathrm{Re}_x^{-1/2}\mathrm{Nu}_x$). Table 4 presents the values of $\mathrm{Re}_x^{1/2}C_f$ and $\mathrm{Re}_x^{-1/2}\mathrm{Nu}_x$ for selected parameter values to analyze their impact for the case when

Table 5 Values of $\mathrm{Re}_x^{1/2}C_f$ and $\mathrm{Re}_x^{-1/2}\mathrm{Nu}_x$ when $\lambda = -1$ and $\phi_1 = \phi_2 = \phi_3 = \phi_4 = 0.005$

S	A	ϕ_5	$\mathrm{Re}_x^{1/2}C_f$		$\mathrm{Re}_x^{-1/2}\mathrm{Nu}_x$	
			1st	2nd	1st	2nd
2	1	0.005	0.720112914	0.320835783	12.160905665	11.926071773
3	1	0.005	0.818160640	0.168106036	18.395960163	18.157755959
4	1	0.005	0.870549058	− 0.176588574	24.580038564	24.298578885
4	2	0.005	0.479158316	− 0.100858424	24.598634117	24.292679935
4	3	0.005	0.330480618	− 0.070650795	24.605634508	24.290269372
4	3	0.010	0.334670588	− 0.071562178	24.568981156	24.249616114
4	3	0.015	0.338930081	− 0.072431203	24.532323466	24.208972677

the sheet is stretched. By providing two initial guesses to the solver, two non-unique solutions were obtained. However, we are confident that typically only the first solution is stable and physically realistic, as demonstrated by most recent studies (for example: [37–44]) though the stability analysis is not yet conducted for the present study. Therefore, the discussion of these results will focus solely on the first solution, though the second solution is provided for future reference. Based on Table 4, focusing on the first solution, it can be observed that as S increases, $\mathrm{Re}_x^{1/2}C_f$ decreases while $\mathrm{Re}_x^{-1/2}\mathrm{Nu}_x$ increases. Conversely, as A increases, $\mathrm{Re}_x^{1/2}C_f$ increases while $\mathrm{Re}_x^{-1/2}\mathrm{Nu}_x$ decreases. These findings indicate that S and A have opposing effects on $\mathrm{Re}_x^{1/2}C_f$ and $\mathrm{Re}_x^{-1/2}\mathrm{Nu}_x$. Hence, the interplay between these two parameters suggests that optimizing one could potentially counteract the effect of the other, making it crucial to consider both parameters simultaneously when controlling the fluid flow system. Further, let us focus on the TiO_2 nanoparticle volume fraction parameter symbolized as ϕ_5. It is observed that as ϕ_5 increases with the use of $A = 3$, both $\mathrm{Re}_x^{1/2}C_f$ and $\mathrm{Re}_x^{-1/2}\mathrm{Nu}_x$ decrease. However, in the case where $A = 1$, an increase in ϕ_5 leads to a decrease in $\mathrm{Re}_x^{1/2}C_f$, but paradoxically causes $\mathrm{Re}_x^{-1/2}\mathrm{Nu}_x$ to increase. Hence, it can be concluded that the penta-hybrid nanofluid can perform optimally by increasing ϕ_5 in a condition of a lesser A. If a larger A is introduced, the heat transfer rate cannot be effectively enhanced through an increase in ϕ_5. It should be noted that this deduction is applicable for the case when the sheet is stretched.

For the case of the shrinking sheet, Table 5 presents the impact of selected parameters on $\mathrm{Re}_x^{1/2}C_f$ and $\mathrm{Re}_x^{-1/2}\mathrm{Nu}_x$. Focusing on the first solution, it can be observed that an increase in S causes both $\mathrm{Re}_x^{1/2}C_f$ and $\mathrm{Re}_x^{-1/2}\mathrm{Nu}_x$ to increase. Meanwhile, an increase in A leads to a decrease in $\mathrm{Re}_x^{1/2}C_f$ but an increase in $\mathrm{Re}_x^{-1/2}\mathrm{Nu}_x$. Conversely, for ϕ_5, an increase in this parameter results in an increase in $\mathrm{Re}_x^{1/2}C_f$ and a decrease in $\mathrm{Re}_x^{-1/2}\mathrm{Nu}_x$. From these observations, it can be deduced that to reduce skin friction, lower values of S and ϕ_5, combined with higher A, are required. On the other hand, achieving a higher heat transfer rate necessitates appropriately higher values of S and A, along with a lower ϕ_5. It is worth noting that the parameter ranges or values considered for the shrinking sheet case differ from those used for the stretching sheet case (refer Table 4). This variation is due to the model's requirement for suitable parameter ranges to ensure numerically accurate solutions, which also implies generating solutions that remain consistently laminar, as the model is designed for laminar flow. Furthermore, we assume that if the generated solutions exhibit significant errors, the

Table 6 Critical values of stretching/shrinking parameter λ_c when $\phi_1 = \phi_2 = \phi_3 = \phi_4 = \phi_5 = 0.005$

S	A	λ_c
2	1	− 2.5676
3	1	− 7.4639
4	1	− 16.2858
2	1	− 2.5676
2	2	− 4.0717
2	3	− 5.5855

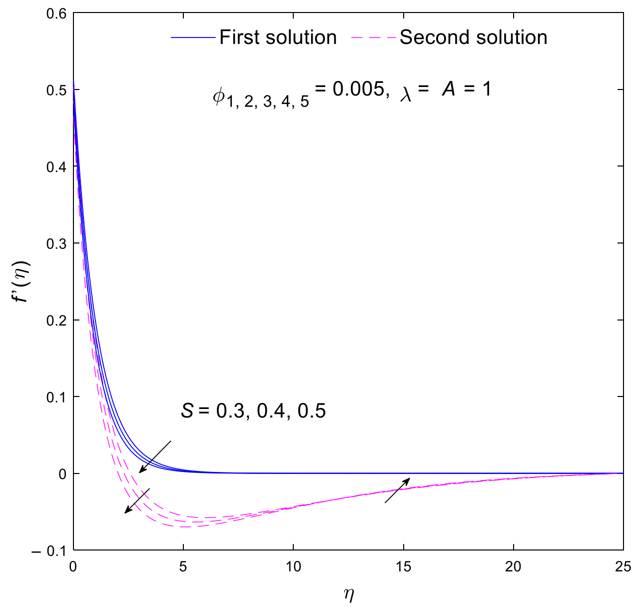

Fig. 2 Velocity profile for variation of suction when the sheet is stretched

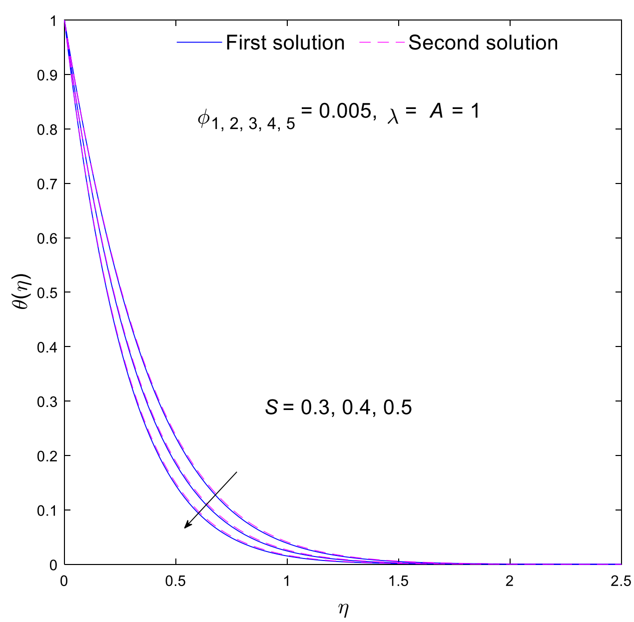

Fig. 3 Temperature profile for variation of suction when the sheet is stretched

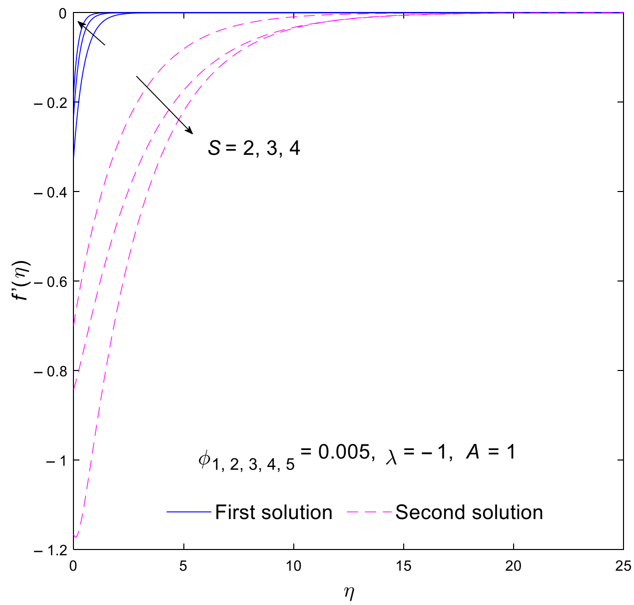

Fig. 4 Velocity profile for variation of suction when the sheet is shrunk

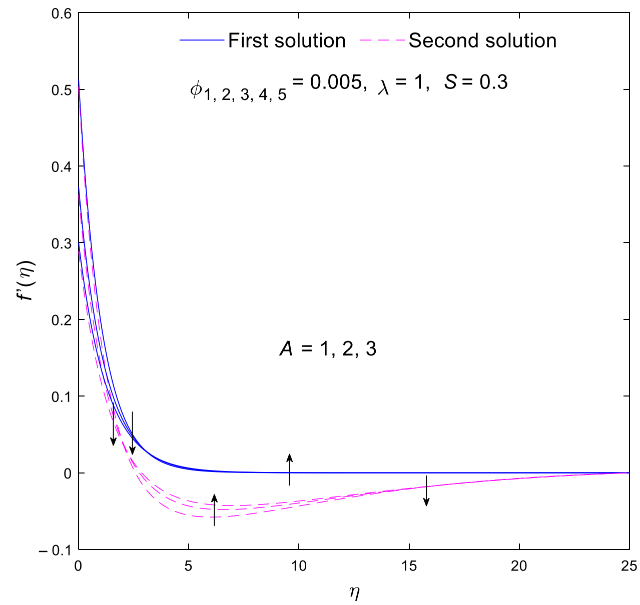

Fig. 6 Velocity profile for variation of velocity slip when the sheet is stretched

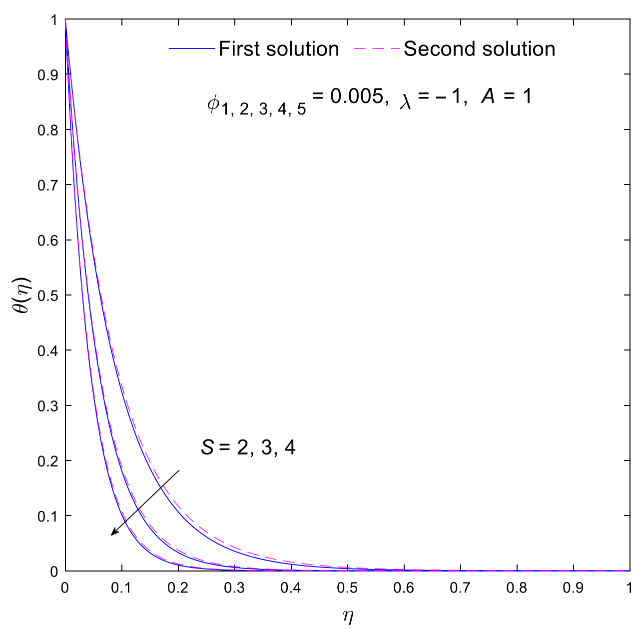

Fig. 5 Temperature profile for variation of suction when the sheet is shrunk

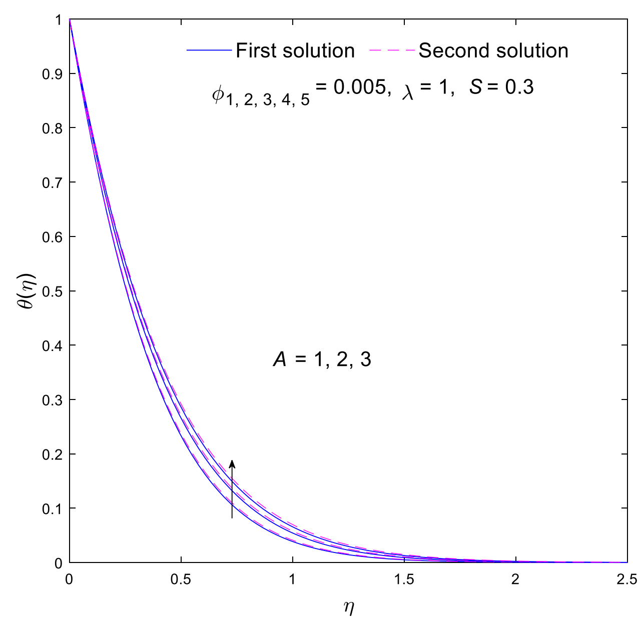

Fig. 7 Temperature profile for variation of velocity slip when the sheet is stretched

solutions may no longer represent the laminar phase and could potentially transit to turbulence.

The importance of generating more than one solution, if possible, lies in the ability to identify critical points that may signify where boundary layer separation could occur. By analyzing these critical points, we can develop strategies to delay boundary layer separation, thereby maintaining laminar flow. Laminar flow is essential for many systems to ensure efficient operation and minimize energy losses. Table 6 presents the critical points for λ for varying values of parameters S and A, which allow us to analyze whether these control parameters can influence boundary layer separation. From Table 6, it is evident that as S increases, the critical point associated with λ decreases. This indicates

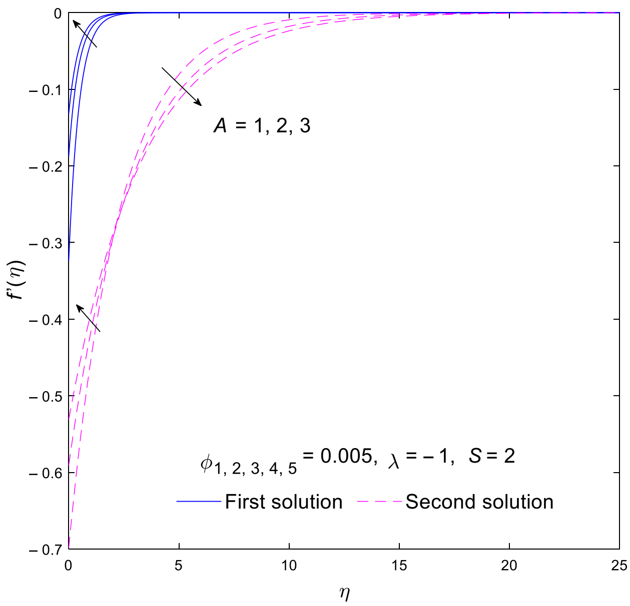

Fig. 8 Velocity profile for variation of velocity slip when the sheet is shrunk

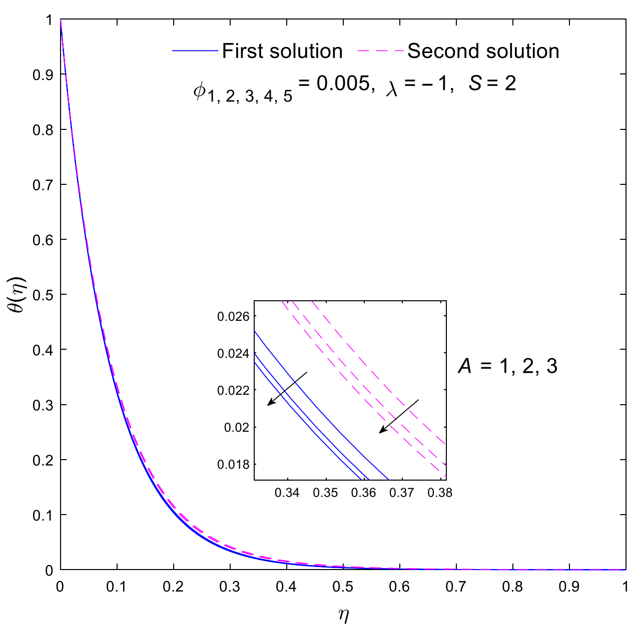

Fig. 9 Temperature profile for variation of velocity slip when the sheet is shrunk

that the range of solutions expands with increasing S up to the critical point, λ_c. Similarly, an increase in A extends the range of λ_c where the sheet can still shrink. Beyond these λ_c, no solution can be generated, signifying that the flow is no longer laminar. This analysis shows that a higher values of S and A can expand the range of shrinking condition of the sheet hence maintained the laminar flow, as specified in Table 6. For instance, if $S = 2$, $A = 1$, and the volume fraction of each nanoparticle is 0.005, the sheet can shrink only up to a critical value of -2.5676. But if S is increased to 4 within the same configuration, the flow can remain in a laminar state up to a shrinking capacity of -16.2858, which significantly expands the solution range. Shrinking the sheet beyond the critical point would cause turbulence, leading to higher energy consumption, reduced efficiency, and instability in systems relying on laminar flow, such as heat exchangers or microfluidic devices. Therefore, operating within the suitable range is essential to maintain performance.

Figures 2–9 illustrate the velocity and temperature profiles of the penta-hybrid nanofluid under various parameter variations within the boundary layer, set with a maximum thickness of 25. Notably, for the thermal boundary layer, the temperature converges much earlier, well before reaching the maximum thickness, indicating that the thermal boundary layer is thinner compared to the momentum boundary layer. Figures 2 and 3 show $f'(\eta)$ and $\theta(\eta)$ for the variation of S under the condition of a stretching sheet. As previously mentioned, we focus solely on the first solution. From the figures, it is evident that under the stretching condition, an increase in suction reduces both the velocity and temperature of the fluid, as well as decreases the thickness of both momentum and thermal boundary layers. Meanwhile, Figs. 4 and 5 show $f'(\eta)$ and $\theta(\eta)$ for the variation of the S under the shrinking condition. The first solution indicates that an increase in suction parameter enhances the velocity while reducing the temperature of the fluid. Additionally, it decreases the thickness of both momentum and thermal boundary layers, for the case when the sheet is shrunk. Further, the impact of A on $f'(\eta)$ and $\theta(\eta)$ is shown in Figs. 6 and 7 (for the stretching sheet case) and Figs. 8 and 9 (for the shrinking sheet case). Focusing on the first solution, we observe that an increase in A for the case of stretching sheet decreases the velocity of the fluid near the boundary while increasing the velocity further from the boundary. Additionally, the temperature increases consistently with A. In contrast, for the shrinking sheet case, an increase in A results in a consistent increase in fluid velocity but a decrease in temperature.

In order to validate the heat transfer rate analysis, we utilize an artificial neural network model through a supervised logic mining method known as S2SATRA [45]. To facilitate this, we generate several random datasets for $\mathrm{Re}_x^{-1/2}\mathrm{Nu}_x$, using different parameter values, in order to perform the logic mining. This logic mining method requires six parameters, with one response which is the heat transfer rate (measured through $\mathrm{Re}_x^{-1/2}\mathrm{Nu}_x$). The data of $\mathrm{Re}_x^{-1/2}\mathrm{Nu}_x$ are generated randomly with different variations of these six parameters. In the first set, we use six parameters that are: silver volume fraction (ϕ_1), gold volume fraction (ϕ_2), magnesium oxide volume fraction (ϕ_3), copper volume fraction

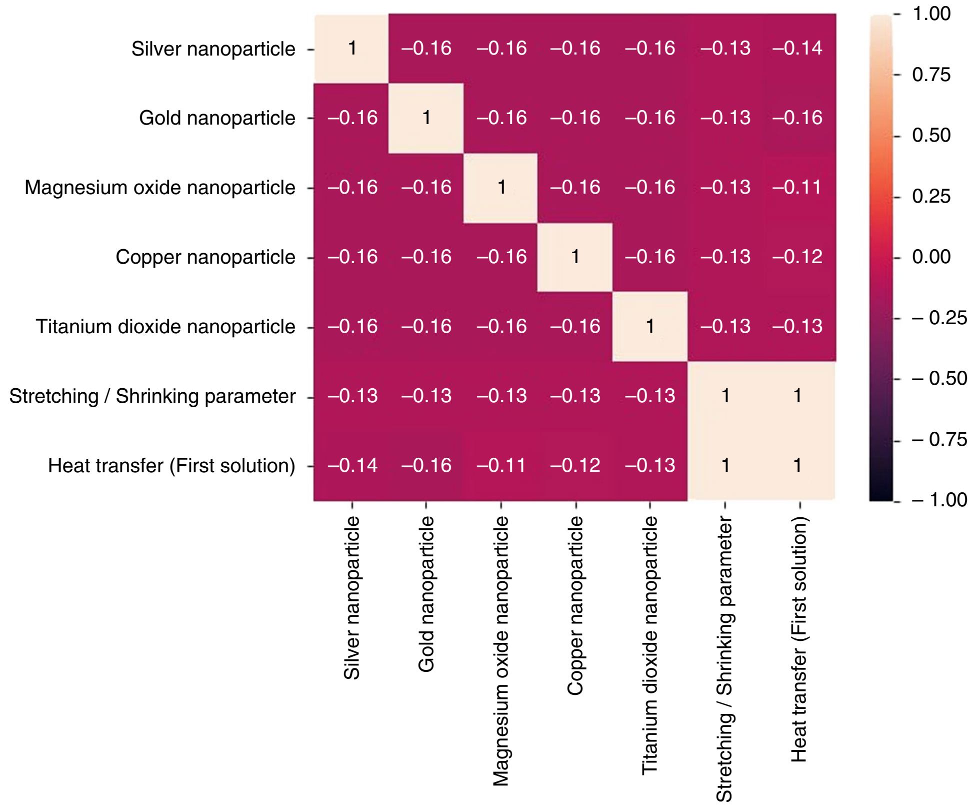

Fig. 10 Correlation heatmap for the first set of parameters corresponds to heat transfer

(ϕ_4), titanium dioxide volume fraction (ϕ_5), and stretching/shrinking (λ), while keeping suction (S) and velocity slip (A) constant with a value of 1. In the second set, we set up six parameters: magnesium oxide volume fraction (ϕ_3), copper volume fraction (ϕ_4), and titanium dioxide volume fraction (ϕ_5), suction (S), stretching/shrinking (λ) and velocity slip (A), while keeping volume fraction for silver (ϕ_1) and gold (ϕ_2) to a constant value of 0.05. Since the boundary layer flow model provides dual numerical solutions, we consider only the first solution for this logic mining, as it is often claimed to be the most stable.

S2SATRA is the extension of conventional 2SATRA with a supervised attribute selection known as correlation analysis. In the correlation analysis, Chi-square analysis is used during the attribute selection stage to identify the best neurons associated with the $\mathrm{Re}_x^{-1/2}\mathrm{Nu}_x$ [46]. The best neurons will contribute to the process of finding the optimal logical rule as shown in Eq. (16) as follows:

$$Q_{2SAT} = \bigwedge_{i=1}^{J} \text{clauses}, \ \text{clauses}_i = \left(A_i \vee B_i\right), \tag{16}$$

where $J=3$. Let the attribute of the dataset is represented by m number of neurons as $S_i = \left(S_1, S_2, .., S_m\right)$ where each neuron is changed into bipolar, $\{-1, 1\}$ [47]. By considering the association between learning logic, Q^{learn} and S_i, we can choose optimal S_i for Q_{2SAT} using Eq. (17) as follows:

$$Q^{\text{learn}} = \bigwedge_{i=0, i\neq j}^{J} \left(S_i^{\min|p_i|} \vee S_j^{\min|p_j|}\right), \tag{17}$$

where p_i is the p value between Q^{learn} and the neuron S_i with range $0 \le p_i \le 0.05$. Figures 10 and 11 show the association of Q^{learn} and S_i for the variables that related to $\mathrm{Re}_x^{-1/2}\mathrm{Nu}_x$. Then, using the selected S_i, we can determine the pair for each clause using Eq. (18):

$$Q_{2SAT}^{\text{best}} = \max\left[n\left(clauses_i\right)\right], \ Q^{\text{learn}} = 1, \tag{18}$$

where $n\left(\text{clauses}_i\right)$ is the number of clauses_i structure that corresponds to $Q^{\text{learn}} = 1$. Noteworthy, Eq. (17) helps S2SATRA to learn early features of the dataset before being implemented in the discrete Hopfield neural network (DHNN). DHNN will produce a final neuron state, S_i^{final}, that corresponds to the selected neurons S_i using Eq. (19):

$$S_i^{\text{final}} = \begin{cases} -1, & HTAF\left[\sum_{i=1, i\neq j}^{m} W_{ij}^{(2)} S_j + W_i^{(1)}\right] < 0 \\ 1, & HTAF\left[\sum_{i=1, i\neq j}^{m} W_{ij}^{(2)} S_j + W_i^{(1)}\right] \ge 0 \end{cases}, \tag{19}$$

The S_i^{final} will be converted back into induced literal based on the following formulation [48]:

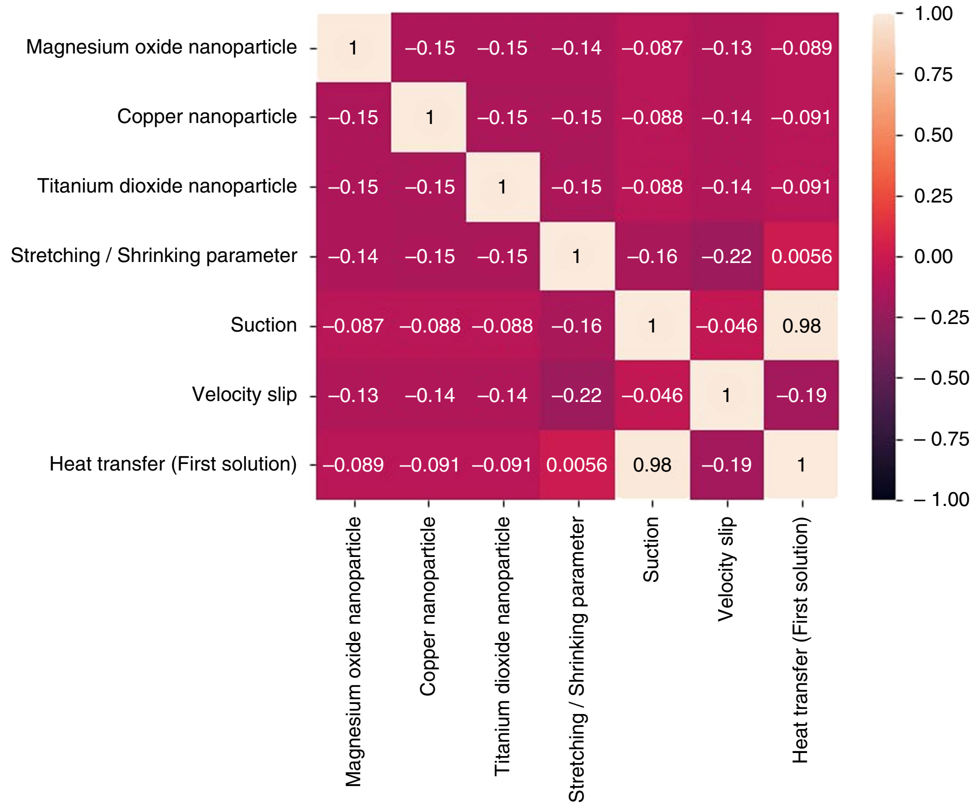

Fig. 11 Correlation heatmap for the second set of parameters correspond to heat transfer

Table 7 Variables in S2SATRA for the first set of parameters

Variable	Representing	Neuron representation via k-mean clustering [49]
A_1	ϕ_1	1: Higher and equal to 0.0044 −1: Lower than 0.0044
B_1	ϕ_2	
A_2	ϕ_3	
B_2	ϕ_4	
A_3	ϕ_5	
B_3	λ	1: Higher and equal to 1.1317 −1: Lower than 1.1317
Γ_{NUX}	$Re_x^{-1/2}Nu_x$ solution	1: Higher and equal to 6.5146 −1: Lower than 6.5146

$$S_i^{induced} = \begin{cases} (\neg A_i \vee \neg B_i), & if\ (S_i, S_j) = (-1, -1) \\ (\neg A_i \vee B_i), & if\ (S_i, S_j) = (-1, 1) \\ (A_i \vee \neg B_i), & if\ (S_i, S_j) = (1, -1) \\ (A_i \vee B_i), & else (S_i, S_j) = (1, 1) \end{cases}. \tag{20}$$

Note that the S2SATRA approach is implemented to validate the numerical findings from the heat transfer analysis that focuses on the first solution (Tables 7, 8).

The results of S2SATRA in classifying the numerical results of $Re_x^{-1/2}Nu_x$ are shown in Tables 9 and 10. As shown in Tables 9 and 10, the value of specificity and Matthew's correlation coefficient is not able to be calculated for some fold because all the $Re_x^{-1/2}Nu_x$ results in that fold are in the positive (1) class. Therefore, two different k-fold cross-validations were implemented to overcome the imbalance class of $Re_x^{-1/2}Nu_x$ results. The best final induced logic extracted is selected based on the highest values of accuracy among all the different logical rules extracted by S2SATRA [50]. Among all the best final induced logic extracted in Tables 9 and 10, the overall relationship between the parameters of $Re_x^{-1/2}Nu_x$ is represented using the best final induced logic with the highest accuracy as in Eq. (21) and Eq. (22) as follows:

$$\text{First set}: Re_x^{-1/2}Nu_x = (\lambda \vee \phi_5) \wedge (\phi_2 \vee \phi_1) \wedge (\phi_3 \vee \neg \phi_4), \tag{21}$$

Table 8 Variables in S2SATRA for the second set of parameters

Variable	Representing	Neuron representation via k-mean clustering [49]
A_1	ϕ_3	1: Higher and equal to 0.0045 −1: Lower than 0.0045
B_1	ϕ_4	1: Higher and equal to 0.0044 −1: Lower than 0.0044
A_2	ϕ_5	
B_2	λ	1: Higher and equal to 1.1539 −1: Lower than 1.1539
A_3	S	1: Higher and equal to 0.8777 −1: Lower than 0.8777
B_3	A	
Γ_{NUX}	$Re_x^{-1/2}Nu_x$ solution	1: Higher and equal to 5.8643 −1: Lower than 5.8643

Table 9 The formulation of final induced logic extracted from S2SATRA for the first set of parameters with accuracy, precision, sensitivity, specificity, and Matthew's correlation coefficient values

k – fold		Final Induced Logic Extracted	Accuracy	Precision	Sensitivity	Specificity	Matthew's Correlation Coefficient
5	1	$(\phi_5 \vee \phi_3) \wedge (\neg\phi_1 \vee \phi_2) \wedge (\lambda \vee \phi_4)$	1.00000	1.00000	1.00000	1.00000	1.00000
	2	$(\lambda \vee \phi_5) \wedge (\phi_1 \vee \phi_3) \wedge (\phi_2 \vee \neg\phi_4)$	1.00000	1.00000	1.00000	1.00000	1.00000
	3	$(\lambda \vee \phi_5) \wedge (\phi_2 \vee \phi_1) \wedge (\phi_3 \vee \neg\phi_4)$	1.00000	1.00000	1.00000	1.00000	1.00000
	4	$(\lambda \vee \phi_4) \wedge (\phi_3 \vee \phi_1) \wedge (\phi_5 \vee \neg\phi_2)$	1.00000	1.00000	1.00000	1.00000	1.00000
	5	$(\phi_4 \vee \lambda) \wedge (\phi_3 \vee \phi_1) \wedge (\neg\phi_2 \vee \phi_5)$	1.00000	1.00000	1.00000	1.00000	1.00000
Average			1.00000	1.00000	1.00000	1.00000	1.00000
Maximum			1.00000	1.00000	1.00000	1.00000	1.00000
10	1	$(\phi_4 \vee \phi_3) \wedge (\phi_1 \vee \lambda) \wedge (\phi_5 \vee \phi_2)$	1.00000	1.00000	1.00000	1.00000	1.00000
	2	$(\lambda \vee \phi_2) \wedge (\phi_3 \vee \neg\phi_5) \wedge (\phi_1 \vee \phi_4)$	1.00000	1.00000	1.00000	1.00000	1.00000
	3	$(\lambda \vee \phi_5) \wedge (\phi_2 \vee \phi_1) \wedge (\phi_3 \vee \neg\phi_4)$	1.00000	1.00000	1.00000	1.00000	1.00000
	4	$(\lambda \vee \phi_1) \wedge (\phi_3 \vee \phi_2) \wedge (\phi_5 \vee \neg\phi_4)$	1.00000	1.00000	1.00000	1.00000	1.00000
	5	$(\phi_1 \vee \phi_3) \wedge (\lambda \vee \phi_4) \wedge (\phi_5 \vee \phi_2)$	1.00000	1.00000	1.00000	–	–
	6	$(\phi_1 \vee \lambda) \wedge (\phi_2 \vee \phi_4) \wedge (\phi_3 \vee \phi_5)$	1.00000	1.00000	1.00000	1.00000	1.00000
	7	$(\lambda \vee \neg\phi_1) \wedge (\phi_4 \vee \phi_2) \wedge (\phi_5 \vee \neg\phi_3)$	1.00000	1.00000	1.00000	1.00000	1.00000
	8	$(\lambda \vee \phi_5) \wedge (\phi_3 \vee \phi_2) \wedge (\phi_1 \vee \neg\phi_4)$	1.00000	1.00000	1.00000	1.00000	1.00000
	9	$(\neg\phi_4 \vee \lambda) \wedge (\phi_5 \vee \phi_2) \wedge (\phi_1 \vee \phi_3)$	1.00000	1.00000	1.00000	1.00000	1.00000
	10	$(\phi_1 \vee \phi_3) \wedge (\lambda \vee \phi_4) \wedge (\phi_5 \vee \phi_2)$	1.00000	1.00000	1.00000	1.00000	1.00000
Average			1.00000	1.00000	1.00000	1.00000	1.00000
Maximum			1.00000	1.00000	1.00000	1.00000	1.00000

$$\text{Second set}: \mathrm{Re}_x^{-1/2}\mathrm{Nu}_x = (S \vee \phi_4) \wedge (\lambda \vee \neg\phi_3) \wedge (A \vee \phi_5). \tag{22}$$

Notably, Eq. (21) is selected based on the repeated induced logic extracted since all the accuracy results in Table 9 are the highest. From Eq. (21), to achieve a higher heat transfer rate, which we consider as 1 (refer Table 7), it follows that $(\phi_1, \phi_2, \phi_3, \phi_4, \phi_5, \lambda) = (1, 1, 1, 1, 1, 1)$. This means that the heat transfer rate is maximized when all the nanoparticle volume fraction parameters: silver (ϕ_1), gold (ϕ_2), magnesium oxide (ϕ_3), copper (ϕ_4), and titanium dioxide (ϕ_5) are set to 1, as well as the stretching/shrinking parameter (λ) (as shown in Table 7). On the other hand, from Eq. (22), to have higher heat transfer rate which we consider for $\mathrm{Re}_x^{-1/2}\mathrm{Nu}_x$ to be 1 (refer Table 8), it gives that $(\phi_3, \phi_4, \phi_5, \lambda, S, A) = (-1, -1, -1, 1, 1, 1)$. The heat transfer is maximized when the volume fraction of magnesium oxide (ϕ_3), copper (ϕ_4), and titanium dioxide (ϕ_5) are set to -1, while suction (S), stretching/shrinking parameter (λ) and velocity slip (A) are set to 1 (as shown in Table 8). From this, through random checks of the numerical data, it is validated that the present boundary layer flow model exhibits the same pattern as given by the resulted (most accurate) induced logic.

Additionally, based on the heatmaps in Figs. 10 and 11, it can be deduced that, for the first set of parameters, the suction parameter shows the highest correlation with the heat transfer rate compared to the other parameters. Meanwhile, for the second set of parameters, the stretching/shrinking parameters exhibit the highest correlation. Mathematically, the suction and stretching/shrinking parameters exhibit the highest correlation because their values are considered sufficiently high in the boundary layer flow model compared to the other parameters, which may explain why they have the most significant effect on the heat transfer rate, in this case. It should be noted here that the effectiveness of S2SATRA as compared to other conventional optimization methods lies in how it selects attributes for the network. In S2SATRA, correlation analysis is used to evaluate and filter out insignificant attributes before the attributes are being trained by the network. Unlike conventional methods, where attributes are selected randomly and potentially cause the network

Table 10 The formulation of final induced logic extracted from S2SATRA for the second set of parameters with accuracy, precision, sensitivity, specificity, and Matthew's correlation coefficient values

k – fold		Final Induced Logic Extracted	Accuracy	Precision	Sensitivity	Specificity	Matthew's Correlation Coefficient
5	1	$(S \vee \lambda) \wedge (\phi_5 \vee \phi_4) \wedge (\phi_3 \vee A)$	0.72165	1.00000	0.68235	1.00000	0.45821
	2	$(\lambda \vee S) \wedge (\phi_5 \vee \phi_3) \wedge (A \vee \phi_4)$	0.72165	1.00000	0.68235	1.00000	0.45821
	3	$(S \vee A) \wedge (\phi_4 \vee \neg \phi_5) \wedge (\phi_3 \vee \lambda)$	0.88660	0.96000	0.84211	0.95000	0.78022
	4	$(S \vee \phi_5) \wedge (\lambda \vee \neg A) \wedge (\phi_4 \vee \phi_3)$	0.79897	0.96850	0.77848	0.88889	0.54564
	5	$(\phi_3 \vee A) \wedge (\phi_4 \vee \lambda) \wedge (\phi_5 \vee S)$	0.81959	1.00000	0.81959	–	–
Average			0.78969	0.98570	0.76098	0.95972	0.56057
Maximum			0.88660	1.00000	0.84211	1.00000	0.78022
10	1	$(S \vee \lambda) \wedge (\phi_3 \vee \phi_5) \wedge (\phi_4 \vee A)$	0.72165	1.00000	0.68235	1.00000	0.45821
	2	$(S \vee \phi_4) \wedge (\lambda \vee \neg \phi_3) \wedge (A \vee \phi_5)$	0.97938	0.96000	1.00000	0.95918	0.95959
	3	$(\phi_4 \vee S) \wedge (\neg \phi_5 \vee \phi_3) \wedge (\lambda \vee A)$	0.88660	0.95122	0.81250	0.95918	0.78104
	4	$(S \vee A) \wedge (\lambda \vee \neg \phi_4) \wedge (\phi_5 \vee \phi_3)$	0.88660	0.96000	0.84211	0.95000	0.78022
	5	$(S \vee \phi_4) \wedge (\phi_5 \vee \neg \lambda) \wedge (A \vee \phi_3)$	0.88660	0.96000	0.84211	–	–
	6	$(S \vee A) \wedge (\lambda \vee \neg \phi_5) \wedge (\phi_4 \vee \phi_3)$	0.79897	0.95918	0.72868	0.93846	0.62983
	7	$(S \vee \phi_4) \wedge (\phi_3 \vee \neg \lambda) \wedge (A \vee \phi_5)$	0.79897	0.96850	0.77848	0.88889	0.54564
	8	$(S \vee A) \wedge (\phi_3 \vee \lambda) \wedge (\phi_5 \vee \phi_4)$	0.80928	1.00000	0.80423	1.00000	0.30942
	9	$(\phi_3 \vee A) \wedge (\phi_5 \vee \lambda) \wedge (S \vee \phi_4)$	0.82474	1.00000	0.82474	–	–
	10	$(\phi_4 \vee \phi_5) \wedge (S \vee \phi_3) \wedge (A \vee \lambda)$	0.81959	1.00000	0.81959	–	–
Average			0.84124	0.97589	0.81348	0.95653	0.63771
Maximum			0.97938	1.00000	1.00000	1.00000	0.95959

Table 11 Summary of the impact of control parameters toward the physical quantities of interest

Control parameters	Sheet condition	Velocity	Temperature	Skin friction	Heat transfer rate	Boundary layer separation
Increment of suction	Stretching	Decrease	Decrease	Decrease	Increase	Delay
	Shrinking	Increase	Decrease	Increase		
Increment of velocity slip	Stretching	Inconsistent	Increase	Increase	Decrease	Delay
	Shrinking	Increase	Decrease	Decrease	Increase	

to train irrelevant attributes and contributed to suboptimal retrieval of final induced logic. This makes S2SATRA superior to conventional methods, as it effectively selects significant attributes and achieved high accuracy classification via the retrieved final induced logic.

Conclusions

In this study, the boundary layer flow of penta-hybrid nanofluid with suction and velocity slip over a stretching/shrinking sheet was investigated. By formulating a mathematical model and solving it numerically using MATLAB's bvp4c solver, the effects of key parameters such as suction, velocity slip, and nanoparticle volume fraction on fluid velocity, temperature, skin friction, and heat transfer rate were explored. It is important to note that penta-hybrid nanofluid with a high concentration of titanium dioxide can significantly enhance the heat transfer rate compared to the lower concentration, particularly only when operating under conditions of lower suction and velocity slip at the boundary, and with the sheet in a stretching condition. However, by regulating just one parameter, the flow characteristics can be significantly influenced, as summarized in Table 11. This table highlights the physical impact of each control parameter on velocity, temperature, skin friction, heat transfer rate, and boundary layer separation.

Further, according to S2SATRA, the analysis identifies the best-induced logic that achieves the highest accuracy in predicting the heat transfer rate, which are: $\mathrm{Re}_x^{-1/2}\mathrm{Nu}_x = (\lambda \vee \phi_5) \wedge (\phi_2 \vee \phi_1) \wedge (\phi_3 \vee \neg \phi_4)$ and $\mathrm{Re}_x^{-1/2}\mathrm{Nu}_x = (S \vee \phi_4) \wedge (\lambda \vee \neg \phi_3) \wedge (A \vee \phi_5)$. Nevertheless, it should be noted also that the findings of this study are based on the simulation of boundary layer flow of penta-hybrid nanofluid over a slip-permeable stretching/shrinking sheet, specifically considering hybridized nanoparticles of silver, gold, magnesium oxide, copper, and titanium dioxide that are dissolved in water. Additionally, the conclusions drawn cannot be guaranteed if different parameter ranges or other nanoparticle combinations are used within the mathematical model. Hence, it is encouraged that the same model be further investigated with different combinations of nanoparticles and across a wider range of parameters to validate and expand the findings of this study.

For future work, other researchers are encouraged to explore optimization techniques, such as response surface methodology (RSM), for this model. Furthermore, applying analytical methods to obtain closed-form solutions would provide additional mathematical insights, while a separate stability analysis would help confirm which of the dual solutions is physically stable.

Acknowledgements All of the authors acknowledged Universiti Putra Malaysia for the given IPM Putra Grant with Project Code: GP-IPM/2024/9806600 and GP-IPM/2024/9787700. The work by I. Pop, has been supported from the Grant PN-III-P4-PCE-2021-0993, UEFISCDI, Romania.

Author contributions Nur Syahirah Wahid did original draft, methodology, formal analysis, writing—review and editing; Nurul Atiqah Romli, Nur Ezlin Zamri performed formal analysis and writing—review and editing; Shahirah Abu Bakar curated the data; Nor Ain Azeany Mohd Nasir done writing—review & editing; Siti Zulaikha Mohd Jamaludin, Mohd Shareduwan Mohd Kasihmuddin, Mohd. Asyraf Mansor: gave the methodology; Norihan Md Arifin, Ioan Pop supervised the article.

Funding Open access funding provided by The Ministry of Higher Education Malaysia and Universiti Putra Malaysia.

Declarations

Conflict of interest No conflict of interest.

References

1. Huminic G, Huminic A. Hybrid nanofluids for heat transfer applications – a state-of-the-art review. Int J Heat Mass Transfer. 2018;125:82–103.
2. Ahmadi MH, Ghazvini M, Sadeghzadeh M, Alhuyi Nazari M, Ghalandari M. Utilization of hybrid nanofluids in solar energy applications: A review. Nano-Struct Nano-Objects. 2019;20: 100386.
3. Jamil F, Ali HM. Chapter 6 - Applications of hybrid nanofluids in different fields. In: Ali HM, editor. Hybrid Nanofluids Convect Heat Transf. Cambridge, Massachusetts: Academic Press; 2020. p. 215–54.
4. Khan ZH, Khan WA, Ibrahim SM, Swain K, Huang Z. Impact of multiple slips and thermal radiation on heat and mass transfer in MHD Maxwell hybrid nanofluid flow over porous stretching sheet. Case Stud Therm Eng. 2024;61: 104906.
5. Mishra SR, Panda S, Baithalu R. Enhanced heat transfer rate on the flow of hybrid nanofluid through a rotating vertical cone: a statistical analysis. Partial Differ Equ Appl Math. 2024;11: 100825.
6. Sarkar A, Mandal G, Pal D. Heat transfer inspection and entropy optimization in water/MoS2-SiO2 Casson hybrid nanofluid flow with quadratic radiation ray over an exponentially contracting permeable Riga surface: duality and stability analysis. Therm Adv. 2024;1: 100003.
7. Khalili Najafabadi M, Hriczó K, Bognár G. Enhancing the heat transfer in CuO-MWCNT oil hybrid nanofluid flow in a pipe. Results Phys. 2024;64: 107934.
8. Gomathi N, Poulomi D. Entropy optimization on EMHD Casson Williamson penta-hybrid nanofluid over porous exponentially vertical cone. Alexandria Eng J. 2024;108:590–610.
9. Alharbi AA. Thermal analysis of heat transport in a slip flow of ternary hybrid nanofluid with suction upon a stretching/shrinking sheet. Case Stud Therm Eng. 2024;54: 103965.
10. Paul A, Sarma N, Patgiri B. Mixed convection of shear-thinning hybrid nanofluid flow across a radiative unsteady cone with suction and slip effect. Mater Today Commun. 2023;37: 107522.
11. Samat NAA, Bachok N, Arifin NM. Hybrid carbon nanotubes flow and heat transfer over a vertical thin needle with suction effect: a numerical and optimisation analysis. Int Commun Heat Mass Transfer. 2024;156: 107702.
12. Jaafar A, Waini I, Jamaludin A, Nazar R, Pop I. MHD flow and heat transfer of a hybrid nanofluid past a nonlinear surface stretching/shrinking with effects of thermal radiation and suction. Chin J Phys. 2022;79:13–27.
13. Wahid NS, Arifin NM, Yahaya RI, Khashi'ie NS, Pop I. Impact of suction and thermal radiation on unsteady ternary hybrid

nanofluid flow over a biaxial shrinking sheet. Alexandria Eng J. 2024;96:132–41.
14. Hammoodi KA, Ayed DJ, Abed MH, Elsheikh A, Flayyih MA, Alizadeh A. Quantitative analysis of heat and mass transfer in MoS2-Al2O3/EG hybrid flow between parallel surfaces with suction/injection by numerical modeling of HPM method. Int J Thermofluids. 2024;24: 100819.
15. Sarma N, Paul A. Engine oil blended Casson hybrid nanofluid flow along a uniformly heated curved surface with Arrhenius activation energy and suction: a computational study. Hybrid Adv. 2024;5: 100161.
16. Badiger AK, Hanumagowda BN, Pavithra KM, Varma SVK, Raju CSK, Noeiaghdam S, et al. Hybrid nanofluid flow over a vertical plate through porous medium in a conducting and chemically reacting field with radiation absorption and variable suction. Results Eng. 2024;24: 103070.
17. Memon MA, Jacob K, Lanjwani HB, Mahmoud EE. Darcy-Forchheimer MHD micropolar water based hybrid nanofluid flow, heat and mass transfer features past on stretching/shrinking surface with slip and radiation effects. Results Eng. 2024;23: 102534.
18. Fatima N, Kousar N, Rehman UK, Shatanawi W. Computational analysis of heat and mass transfer in magnetized Darcy-Forchheimer hybrid nanofluid flow with porous medium and slip effects. Comput Model Eng Sci. 2023;137:2311–30.
19. Jamrus FN, Waini I, Khan U, Ishak A. Effects of magnetohydrodynamics and velocity slip on mixed convective flow of thermally stratified ternary hybrid nanofluid over a stretching/shrinking sheet. Case Stud Therm Eng. 2024;55: 104161.
20. Hashim AS, Rehman S, Alshehery S, Bibi S. Computational investigation of magnetized hybrid nanofluids heat transport and flow through elongational surface with thermal radiation and wall slip. Heliyon. 2023;9: e20056.
21. Mahmood Z, Rafique K, Khan U, Abd El-Rahman M, Alharbi R. Analysis of mixed convective stagnation point flow of hybrid nanofluid over sheet with variable thermal conductivity and slip Conditions: a Model-Based study. Int J Heat Fluid Flow. 2024;106:109296.
22. Panda S, Baithalu R, Baag S, Mishra SR. Behaviour of effective heat transfer rate in radiating micropolar nanofluid over an expanding sheet with slip effects. Partial Differ Equ Appl Math. 2024;11: 100851.
23. Usafzai WK, Aly EH, Pop I. Multiple exact solutions in tri-hybrid nanofluid flow: a study of elastic surface effects. Int J Numer Methods Heat Fluid Flow. 2025;35:277–99.
24. Mahabaleshwar US, Maranna T, Pérez LM, Bognár GV, Oztop HF. An impact of radiation on laminar flow of dusty ternary nanofluid over porous stretching/shrinking sheet with mass transpiration. Results Eng. 2023;18: 101227.
25. Mahros AM, Aly EH. Comparative study for heat transfer characteristics of many graphene hybrid nanofluids flow over a shrinking sheet. Chin J Phys. 2024;92:416–31.
26. Roy NC, Hossain A, Pop I. Flow and heat transfer of MHD dusty hybrid nanofluids over a shrinking sheet. Chin J Phys. 2022;77:1342–56.
27. Kaswan P, Kumar M, Kumari M, Mandal G. Stability analysis of dual solutions for nonlinear radiative magnetohydrodynamic flow of $Ag-TiO_2/H_2O$ hybrid nanofluid over a nonlinearly shrinking surface. Therm Adv. 2024;1: 100002.
28. Rafique K, Mahmood Z, Khan U, Muhammad T, Mir A, et al. Unsteady MHD flow analysis of hybrid nanofluid over a shrinking surface with porous media and heat generation: computational study on entropy generation and Bejan number. Int J Heat Fluid Flow. 2024;107:109419.
29. Alkasasbeh HT, Mohamed MKA. MHD (SWCNTS + MWCNTS)/H_2O-based Williamson hybrid nanouids flow past exponential shrinking sheet in porous medium. Front Heat Mass Transf. 2023;21:265–79.
30. Jain R, Mehta R, Bhatnagar A, Ahmad H, Khan ZA, Ismail GM. Numerical study of heat and mass transfer of Williamson hybrid nanofluid (CuO/CNT's-water) past a permeable stretching/shrinking surface with mixed convective boundary condition. Case Stud Therm Eng. 2024;59: 104313.
31. Devi SU, Devi SA. Heat transfer enhancement of $Cu-Al_2O_3$/water hybrid nanofluid flow over a stretching sheet. J Nigerian Math Soc. 2017;36:419–33.
32. Waini I, Ishak A, Pop I. Hybrid nanofluid flow and heat transfer past a permeable stretching/shrinking surface with a convective boundary condition. J Phys Conf Ser. 2019;1366: 012022.
33. Wahid NS, Zamri NE, Jamaludin SZM, Norzawary NHA, Kasihmuddin MSM, Mansor MohdA, et al. Melting ternary hybrid nanofluid stagnation point flow with velocity slip past a stretching/shrinking sheet: numerical simulation and validation via P2SATRA. Alexandria Eng J. 2025;112:74–83.
34. Manjunatha S, Puneeth V, Gireesha BJ, Chamkha AJ. Theoretical study of convective heat transfer in ternary nanofluid flowing past a stretching sheet. J Appl Comput Mech. 2022;8:1279–86.
35. Jakeer S, Reddy SRR, Rashad AM, Lakshmi Rupa M, Manjula C. Nonlinear analysis of Darcy-Forchheimer flow in EMHD ternary hybrid nanofluid (Cu-CNT-Ti/water) with radiation effect. Forces Mech. 2023;10: 100177.
36. Usafzai WK, Aly EH, Alshomrani AS, Ullah MZ. Multiple solutions for nanofluids flow and heat transfer in porous medium with velocity slip and temperature jump. Int Commun Heat Mass Transfer. 2022;131: 105831.
37. Wahid NS, Arifin NM, Mohd Nasir NAA, Pop I. Ternary hybrid nanofluid with first and second order velocity slips: dual solutions with stability analysis. Comput Model Eng Sci. 2025;142:1865–81.
38. Yahaya RI, Mustafa MS, Md Arifin N, Md Ali F, Mohamed Isa SSP. Heat transfer optimization for the unsteady mixed convection flow of hybrid nanofluid over a permeable EMHD riga plate with thermal radiation and convective boundary condition. Multiscale Multidiscip Model Exp Des. 2025. https://doi.org/10.1007/s41939-025-00758-7.
39. Yahaya RI, Md Arifin N, Mustafa MS, Pop I, Md Ali F, Mohamed Isa SSP. Mixed convection hybrid nanofluid flow past a non-isothermal cone and wedge with radiation and convective boundary condition: Heat transfer optimization. Case Stud Therm Eng. 2025;66: 105768.
40. Khashi'ie NS, Waini I, Arifin NM, Pop I. Dual solutions of unsteady two-dimensional electro-magneto-hydrodynamics (EMHD) axisymmetric stagnation-point flow of a hybrid nanofluid past a radially stretching/shrinking Riga surface with radiation effect. Int J Numer Methods Heat Fluid Flow. 2023;33:333–50.
41. Khashi'ie NS, Arifin NM, Rosca NC, Rosca AV, Pop I. Three-dimensional flow of radiative hybrid nanofluid past a permeable stretching/shrinking sheet with homogeneous-heterogeneous reaction. Int J Numer Methods Heat Fluid Flow. 2022;32:568–88.
42. Wahid NS, Arifin MN, Khashi'ie NS, Pop I, Bachok N, Hafidzuddin EH. Three-dimensional stretching/shrinking flow of hybrid nanofluid with slips and Joule heating. J Thermophys Heat Transf. 2022;36:1–10.

43. Khashi'ie NS, Arifin NM, Pop I, Wahid NS. Effect of suction on the stagnation point flow of hybrid nanofluid toward a permeable and vertical Riga plate. Heat Transf. 2021;50:1895–910.
44. Wahid NS, Arifin NM, Khashi'ie NS, Pop I. Mixed convection of a three-dimensional stagnation point flow on a vertical plate with surface slip in a hybrid nanofluid. Chin J Phys. 2021;74:129–43.
45. Kasihmuddin MSM, Jamaludin SZM, Mansor MohdA, Wahab HA, Ghadzi SMS. Supervised learning perspective in logic mining. Mathematics. 2022;10: 915.
46. Rusdi NA, Kasihmuddin MSM, Romli NA, Manoharam G, Mansor MA. Multi-unit Discrete Hopfield Neural Network for higher order supervised learning through logic mining: Optimal performance design and attribute selection. J King Saud Univ - Comput Inf Sci. 2023;35:101554.
47. Zamri NE, Mansor MA, Kasihmuddin MSM, Sidik SS, Alway A, Romli NA, et al. A modified reverse-based analysis logic mining model with Weighted Random 2 Satisfiability logic in Discrete Hopfield Neural Network and multi-objective training of Modified Niched Genetic Algorithm. Expert Syst Appl. 2024;240:122307.
48. Romli NA, Zulkepli NFS, Kasihmuddin MSM, Zamri NE, Rusdi NA, Manoharam G, et al. Unsupervised logic mining with a binary clonal selection algorithm in multi-unit discrete Hopfield neural networks via weighted systematic 2 satisfiability. AIMS Math. 2024;9:22321–65.
49. Manoharam G, Kassim AM, Abdeen S, Kasihmuddin MSM, Rusdi NA, Romli NA, et al. Special major 1, 3 satisfiability logic in discrete Hopfield neural networks. AIMS Math. 2024;9:12090–127.
50. Alway A, Zamri NE, Mansor MA, Kasihmuddin MSM, Jamaludin SZM, Marsani MF. A novel Hybrid Exhaustive Search and data preparation technique with multi-objective Discrete Hopfield Neural Network. Decis Anal J. 2023;9:100354.